Individual-based and continuum models of growing cell populations: a comparison

Helen Byrne · Dirk Drasdo

Abstract   In this paper we compare two alternative theoretical approaches for simulating the growth of cell aggregates in vitro: individual cell (agent)-based models and continuum models. We show by a quantitative analysis of both a biophysical agent-based and a continuum mechanical model that for densely packed aggregates the expansion of the cell population is dominated by cell proliferation controlled by mechanical stress. The biophysical agent-based model introduced earlier (Drasdo and Hoehme in Phys Biol 2:133–147, 2005) approximates each cell as an isotropic, homogeneous, elastic, spherical object parameterised by measurable biophysical and cell-biological quantities and has been shown by comparison to experimental findings to explain the growth patterns of dense monolayers and multicellular spheroids. Both models exhibit the same growth kinetics, with initial exponential growth of the population size and aggregate diameter followed by linear growth of the diameter and power-law growth of the cell population size. Very sparse monolayers can be explained by a very small or absent cell–cell adhesion and large random cell migration. In this case the expansion speed is not controlled by mechanical stress but by random cell migration and can be modelled by the Fisher–Kolmogorov–Petrovskii–Piskounov (FKPP) reaction–diffusion equation. The growth kinetics differs from that of densely packed aggregates in that the initial spread, as quantified by the radius of gyration, is

H. Byrne
School of Mathematical Sciences, University of Nottingham,
Nottingham NG7 2RD, UK
e-mail: helen.byrne@nottingham.ac.uk

D. Drasdo (✉)
INRIA, Domaine Rocquencourt, B.P. 105, 78153 Le Chesnay Cedex, France
e-mail: dirk.drasdo@inria.fr

D. Drasdo
IZBI, University of Leipzig, Leipzig, Germany

diffusive. Since simulations of the lattice-free agent-based model in the case of very large random migration are too long to be practical, lattice-based cellular automaton (CA) models have to be used for a quantitative analysis of sparse monolayers. Analysis of these dense monolayers leads to the identification of a critical parameter of the CA model so that eventually a hierarchy of three model types (a detailed biophysical lattice-free model, a rule-based cellular automaton and a continuum approach) emerge which yield the same growth pattern for dense and sparse cell aggregates.

1 Introduction

Many aspects of tumour and tissue growth have been studied using mathematical models. In many cases deterministic models of the reaction–diffusion type or continuum mechanical models have been used (for a comprehensive review see [1,10,51, 65] and references therein). These are well suited to the description of large scale phenomena where the cell and tissue properties vary smoothly over a length scale of several cell diameters. In this paper we focus on the growth of cell populations in vitro. Continuum models which have used to address this issue assume that growth is mechanically regulated [6,20] or nutrient-limited and have also focused on the role of cell–cell interactions [13,17]. The analysis of these models, demonstrating that they are well-posed and admit unique solutions, raises several challenging issues which are now being investigated [41].

In order to study small-scale phenomena or situations in which the properties of the cells vary over distances comparable to the size of a cell, single-cell-based models permit a higher degree of spatial resolution than models in which sub-cellular properties are replaced by locally averaged quantities. Most individual-based models can be characterised as either lattice-based or lattice-free models (for reviews, see [3,8,33,58]). In some lattice models, each lattice site can be occupied by at most one cell (e.g., [2,9,12,31,34]) while in others one cell may span many lattice sites (e.g. [26,45,47,54,71]). Within the class of lattice-free models, cells have been parameterised by measurable cell-biophysical and cell-biological parameters and approximated by deformable spheres or ellipses (e.g. [29,37–40,43,42,64,61,67]) and, more recently, in a multi-centre approach by aggregates of spheres [60].

When simulating processes associated with developmental biology or growing tumours one is often interested in systems which evolve from a single progenitor cell to $O(10^6)$ cells in vitro and in excess of $O(10^{11})$ in vivo. Such large cell population sizes are not amenable to investigation using agent-based models. Additionally, it is often neither necessary nor desirable to track the fate of every individual cell within large populations. A continuum approach is better suited to modelling such scenarios. Unfortunately, it is often difficult to relate the parameters of the continuum model to those of the individual-based model. Consequently, it is unclear if the behaviour

observed in the continuum model is the same as the behaviour that would have been obtained from a large scale simulation with the individual-based model used to model the same biological system on small scales.

Since much experimental data about cells is collected at the cellular and sub-cellular levels, ideally, what is needed is a rigorous derivation of large-scale continuum models from individual-based models that are based on well-founded experimental information. In this way it should be possible to ensure that small-scale properties relevant for the large scales are retained and error estimates quantifying the validity of the continuum equations at finite population sizes are stated [30,70]. However, existing mathematical techniques permit rigorous derivations of continuum models from agent-based models in only a very limited number of cases.

In cases for which it is not possible to relate the agent-based and continuum models at intermediate population sizes, some progress can be made by comparing their spatial-temporal dynamics: this is the approach we adopt in this paper. While we focus on compact monolayers, growing on a flat substrate, the models can readily be extended to three dimensions as we illustrate in Appendix B.

As shown previously [38,43], cell populations on flat substrates may be classified broadly by three phenotypes (Fig. 1):

– **Type I**: such cells grow as perfect (or near-perfect) compact monolayers (e.g., HTC100-cells and rat astrocytes) (Fig. 1a); Here, the growth is assumed to be controlled by a biomechanical form of contact inhibition. Growth by contact inhibition has been studied by both individual-based approaches (e.g. [34,37,39, 43,44]) and continuum models (e.g. [22]). In both approaches a growth behaviour corresponding to a travelling front has been found. If cell–cell adhesion is strong then the cell population forms a sharp interface with its environment at each size of the population. The effect of cell–cell adhesion has been studied by both individual-based approaches (e.g. [34,37,39,40,43,44]) and continuum
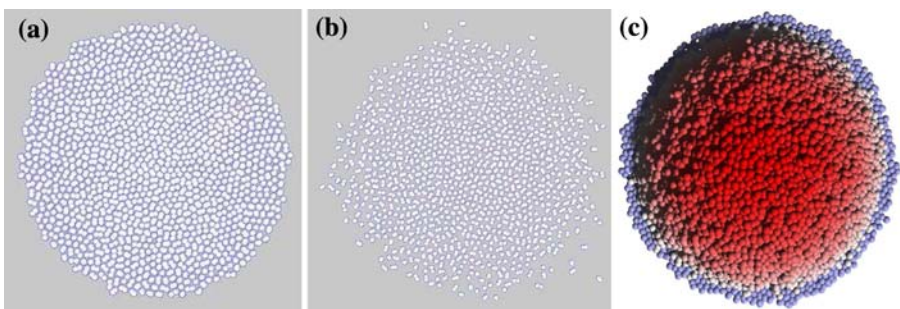

Fig. 1 Typical cell population phenotypes. **a** Cell–cell adhesion is strong enough to maintain the integrity of the cell layer (type I), **b** when cell–cell adhesion is very weak or completely absent the cells initially form a loose clump of cells (type II), and **c** here cell–cell adhesion ensures the integrity of the cell aggregate but control mechanisms such as contact-inhibition of growth, substrate-contact-dependent growth control and substrate-contact-dependent apoptosis are absent (type III). In **c**, *blue* cells are in direct contact with the substrate, while the *dark red* cells are at the greatest distance from the substrate. (All figures were obtained from simulations with the individual-based off-lattice model described in the text or slight modifications of if. For further details see text.)

approaches (e.g. [17,19,41]) as well. The continuum approaches partly considered nutrient limitations (e.g. [72]) and partly biomechanical control as limiting (e.g. [6,7,63]).

– **Type II:** these cells are highly migratory, with negligible (or no) cell–cell adhesion (*e.g.* NIH3T3-cells [69]). Initially they grow as a disperse, non-compact monolayer and only after about two weeks do they start to become increasingly dense and resemble the type I-monolayer (Figs. 1b, 8);

– **Type III:** cells of this type (e.g., WiDr-cells) initially form a compact monolayer as in type I. However, when the monolayer reaches a certain size, the cells start to pile up and extend in the direction perpendicular to the plane of the monolayer [38,43] (Fig. 1c).

We consider monolayer growing on a flat substrate not surrounded by a tissue-like medium or another cell clone (these could modify both the growth kinetics and the shape of the monolayer [32,37,38,44]).

In this paper we compare the results of computer simulations from an individual-based lattice-free ("off-lattice") model that has recently been used to generate quantitative simulations of monolayers and multi-cellular spheroids [34,37,43] with an analysis of a continuum model, both models specialised to describe type I monolayers.

In Sect. 2 we present both approaches and show that they predict the same qualitative growth dynamics.

For type II monolayers, the computational time taken to perform lattice-free agent-based models prohibits a systematic parameter analysis, particularly if the cells are assumed to be highly motile. For this reason we have recently developed a cellular automaton (CA) model that exhibits the same growth behaviour as the lattice-free agent-based model and is much simpler to simulate [12]. We have used this CA model to derive a continuum model that is valid on large scales and showed, by a systematic derivation, that on large scales the system behaviour of the cellular automaton model can well be described by a stochastic form of the Fisher–Kolmogorov–Petrovskii–Piskounov (FKPP)-equation [34]. In Sect. 3 we introduce both the CA model and its associated FKPP-equation. Both models contain a parameter, the "proliferation depth", which accounts for cells that divide inside the proliferating rim and forces outside cells to rearrange into (or, align themselves in) the direction of the tumour-medium interface. We conclude Sect. 3 by showing how the analysis of the continuum and lattice-free agent-based models enables us to determine the dependence of the proliferation depth on other model parameters. In this way our analysis of type I monolayers helps to improve the models of type II monolayers and, in particular, facilitates predictions of the CA model and its associated FKPP-equation.

2 Dense phenotype (type I)

We start by introducing the individual-based lattice-free model in which the basic unit is the single cell. Each cell is represented as an elastic, sticky object which can migrate, change its orientation, grow and divide. The model is parameterised by measurable biophysical, cell-biological and cell-kinetic parameters. We present computer simulations with this model in which the growth rate of the cells is varied. Our observables

are the cell population size, the radius of gyration of the monolayer (a robust measure of the radius) and the thickness of the proliferating rim. We then present a continuum model which exhibits the same growth kinetics as the agent-based model at small and long times. We show further that the agent-based and continuum models predict the same (non-trivial) dependence of the monolayer diameter growth velocity on the cell proliferation rate at long times.

2.1 The individual-based model

Model assumptions: For the agent-based model we make the following assumptions:

(A1) Since isolated cells in culture or free suspension often have a spherical shape we assume each model cell to be spherical directly after cell division. Cells that do not continue to grow and divide (to proliferate) are assumed to maintain their spherical shape. Proliferating cells grow and deform into a dumb-bell during mitosis until they stepwise divide into two spherical daughter cells of equal size (Fig. 2a). The number of steps needed to complete the cell cycle together with the average step size and a reference timescale determine the intrinsic cycle time (the duration of the cell cycle in the absence of any cell–cell interaction). For details, see Appendix A. We assume that cell–substrate adhesion is large enough to prevent cells from being pushed out of the layer. As shown in [38,43], monolayers do not pile up at realistic cell–substrate adhesion strengths as long as the growth control mechanisms of contact inhibition, anchorage-dependent proliferation and anchorage-dependent apoptosis are functioning. In this case we can assume that the dumb-bell axis remains within a plane parallel to the substrate surface.
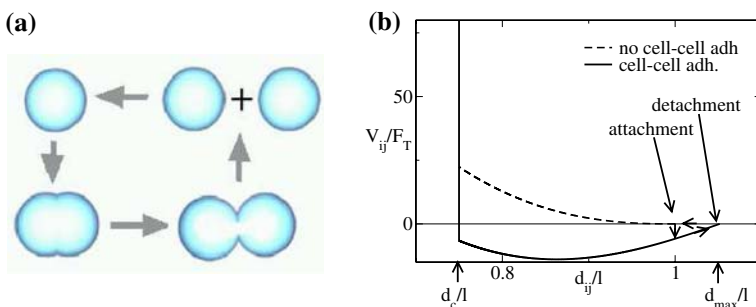

Fig. 2 **a** Sketch of cell division in our individual-based off-lattice model. A parent cell of radius r_c deforms, in steps of size $\delta a \ll r$, into a dumb-bell containing two daughter cells both of radius $r_c = l/2$ (l: cell diameter). **b** Interaction potential energies vs. distance d_{ij} of the centres of the closest dumb-bell spheres for the JKR model in the presence (*dashed lines*) and absence (*full lines*) of cell–cell adhesion, and for pure hard core repulsion. Cells cannot get closer to each other than the minimum distance d_c/l which mimics the limited cell compressibility. Note the hysteresis behaviour in the presence of cell–cell adhesion: cell–cell detachment occurs at distances $d_{max} > l$ larger than cell–cell attachment. For the curve with cell–cell adhesion we used the parameters $W_s = 25k_BT$ at $T = 300$ K [11], $\varrho_m = 10^{15}/m^2$ [24,62], $E = 400$ Pa [56] and $\nu = 0.4$ [53] for cells i, j. Further we assume $l = 10\,\mu$m for the cell diameter. For the curve without cell–cell adhesion, $\varrho_m = 0$ while the other parameters are the same as those for the curve with cell–cell adhesion

(A2) Cells in contact can form adhesive bonds. With decreasing distance between the centres of two cells (e.g., upon compression), both their contact area and the number of adhesive contacts increase, resulting in an attractive interaction. On the other hand, if cells are spheroidal in isolation, a large contact area between them significantly stresses their cytoskeleton and membranes. Furthermore, experiments suggest that cells only have a small compressibility (the Poisson numbers are in the range 0.33–0.5 [4,53]). The limited deformability and compressibility give rise to a repulsive interaction. We model the combination of repulsive and attractive energy contributions with the Johnson–Kendall–Roberts model [48]. This model describes the interaction between two homogeneous elastic, isotropic, adhesive spheres and has recently been shown to give a good description of the attachment and detachment forces of murine sarcoma S180 cells [25]. The model represents the hysteresis effect between cell–cell attachment and cell–cell detachment. Cell–cell attachment: when two cells of radius r_c approach each other they spontaneously form a contact area of finite size at distance $d_{ij} = 2r_c = l$ while if $d_{ij} > 2r_c$ there is no contact. Cell–cell detachment: when the two cells are pulled apart they maintain contact if the distance d_{ij} that separates them lies in the interval $2r_c \leq d_{ij} \leq d_{\max}$. The total cell–cell interaction energy V_{ij} between cells i and j is (see Fig. 2b [37]):

$$
V_{ij} = \begin{cases}
\infty & \text{if } d_{ij} \leq d_c, \\
V_{ij}^{(JKR)} & \text{if } d_c < d_{ij} \leq l \quad \text{(attachment)}, \\
0 & \text{if } l < d_{ij} \quad \text{(attachment)}, \\
V_{ij}^{(JKR)} & \text{if } d_c < d_{ij} \leq d_{\max} \quad \text{(detachment)}, \\
0 & \text{if } d_{\max} < d_{ij} \quad \text{(detachment)}.
\end{cases}
\tag{1}
$$

The interaction energy $V_{ij}^{(JKR)}$ is related to the force $\underline{F}_{ij}$ via

$$
\underline{F}_{ij} = -\underline{\nabla} V_{ij}^{(JKR)}
$$

The force $F_{ij} \equiv |\underline{F}_{ij}(d_{ij})|$ in the JKR-model is determined numerically from the implicit equation [21]:

$$
\delta = \frac{a^2}{\tilde{r}} - \left[4\pi \sigma a (1 - v^2)/\tilde{E} \right]^{1/2},
\tag{2}
$$

in which

$$
a^3 = \frac{3(1 - v^2)\tilde{r}}{2\tilde{E}} \left[F_{ij} + 3\pi\sigma\tilde{r} + \left[6\pi\sigma\tilde{r}F_{ij} + (3\pi\sigma\tilde{r})^2 \right]^{1/2} \right].
\tag{3}
$$

$\tilde{r}^{-1} = \frac{1}{r_i} + \frac{1}{r_j}$, $d_{ij} = r_i + r_j - \delta$, $\tilde{E}^{-1} = \left(\frac{1-v_i^2}{E_i} + \frac{1-v_j^2}{E_j} \right)$, and E_i, E_j are the Young moduli, v_i, v_j the Poisson numbers of cells i and j, respectively. In addition, $r_i = l_i/2$ is the cell radius and we assume $r_i = r_c =$ constant for all cells i. The parameter δ denotes the central displacement and measures the deformation of two interacting cells along the axis that connects the centres of the nearest spheres of the neighbouring dumb-bells i, j. $\sigma \approx \varrho_m W_s$, where ϱ_m is the density of surface adhesion molecules in the contact zone [24,62], W_s is the binding energy of a single bond, a is the radius of the contact area A_c and $A_c = \pi a^2$.

(A3) In the absence of chemotactic signals, isolated cells in suspension or culture medium have been observed to perform a random walk [57,68]. We model this by a stochastic component in the movement of each cell which we characterise by the cell diffusion constant D.

(A4) While in mechanical contact to other cells, proliferating cells exert a (cell) pressure on their neighbours. The neighbouring cells try to escape this pressure by moving against the friction caused by the other neighbour cells and extracellular material (e.g. matrix). The stronger the friction, the slower the cells move. We simulate a friction-dominated stochastic dynamics driven by physical interactions by the standard Metropolis algorithm [55] with a proper definition of timescales (e.g. [36,39]). Note that the movement may be active or passive or both. The observations in Ref. [59], however, suggest that on a flat substrate cells migrate rather than being pushed by dividing cells. The algorithm uses the interaction energy (Eq. 1, see also Fig. 2b), that can directly be related to forces. In our two-dimensional monolayer simulations we perform on average one translation trial of size ξ and one orientation trial of angle $\delta\alpha$ per cell within each time period Δt and accept it with probability $P_a = 1$ if $\Delta V^{\text{tot}} = V_{t+\Delta t}^{\text{tot}} - V_t^{\text{tot}} < 0$ and with probability $P_a = \exp(-\Delta V^{\text{tot}}/F_T)$ otherwise. α is the rotation angle of the dumb-bell axis in the substrate plane. This algorithm can easily be extended to three dimensions (Appendix A). ξ and $\delta\alpha$ are random variables distributed uniformly in the intervals $\xi \in [0, \xi_{\text{max}})$ and $\delta\alpha \in (-\delta\alpha_{\text{max}}, \delta\alpha_{\text{max}})$, respectively. Each translation step trial is performed into a random direction. $\xi_{\text{max}} \ll l$, $\delta\alpha_{\text{max}} \ll \pi$. Here, $V^{\text{tot}} = \sum_{i<j}^N V_{ij}$ summarises the attractive and repulsive cell–cell interactions between all cells, V_{ij} denotes the interaction between cells i and j (Fig. 2b). Every $n_g \gg 1$ translation and orientation trials, one growth trial of size δa uniformly distributed in $[0, \delta a_{\text{max}})$ is performed. $F_T \approx 10^{-16}$ is a reference energy [11] analogous to the thermal energy $k_B T$ in fluids or gases (T: temperature, k_B: Boltzmann constant). In order to use the Monte Carlo method for kinetic simulations we have defined time scales for each of the processes growth, division, migration and rotation.

We have recently illustrated for selective examples that the Metropolis-based simulation method leads to the same dynamics as those obtained from Langevin equations of motion for each individual cell [38]. The Metropolis-based dynamic algorithm used here can be interpreted as a numerical integration of a master equation for the multicellular configuration [35].

(A5) This model does not explicitly consider a cell cycle check point. Instead we assume that cells do proceed growing if a growth step would reduce the cell–cell distance to $d_{ij} < d_c$. This is embodied in the interaction potential energy (Fig. 2b). For selected simulations without an assumption of a hard core and with the assumption of an explicit checkpoint at the $G_1 \rightarrow S$ transition we obtained the same results (Drasdo and Hoehme, unpublished data) which justifies our model assumption made here. The reason for this is that cells under strong compression do almost not contribute to the increase of the cell population size so it does not matter whether they stop in any of the cell cycle check points or remain in the cell cycle but do not or almost not grow.

The local force threshold at which cells stop to proliferate hence is $F_{ij}(d_{ij} \longrightarrow_{\epsilon \rightarrow 0} d_c + \epsilon)$ (here ϵ is a small parameter) and can directly be investigated from the potential energy using $F_{ij} = -\partial V / \partial d_{ij}$. The corresponding (cell) pressure is given by $p_0^{(ij)} = F_{ij}/(\pi a^2(F_{ij}))$ which can be calculated from Eq. (3). Biologically this assumption models a biomechanical form of contact inhibition.

2.1.0.1 Simulation results We use this model for a cell–cell adhesion strength that guarantees cell detachment is prohibited. Each simulation starts with a single cell. As already shown in previous simulations (e.g. [37]) the initial growth of both, the cell population size and the monolayer radius is exponentially fast for type-I monolayers crossing over to a linear growth of the monolayer diameter L and a $N \propto t^2$ (in d spatial dimensions: $N \propto t^d$). Figure 3 shows typical simulation results for different cell length durations. Instead of the monolayer radius, we used the radius of gyration, defined by

$$R_{gyr} = \sqrt{\frac{1}{N} \sum_{i=1}^{N} (\underline{r}_i - \underline{R}_{cm})^2}, \qquad (4)$$

where $\underline{R}_{cm} = \sum_{i=1}^{N} \underline{r}_i$ denotes the position of the centre of mass. For dense, approximately circular cell monolayers, the radius of the monolayer is $R = L/2 \approx \sqrt{2} R_{gyr}$. Firstly we investigated the expansion velocity in the asymptotic linear growth regime by $v = dR/dt$ (Fig. 6a). In a second step we investigated the thickness of the proliferating rim. We used different definitions of the thickness of the proliferating rim. Firstly, we investigate the thickness of the proliferating rim from the growth kinetics in the linear growth regime by $\Delta L = v\tau$ where $v = dR/dt$ denotes the expansion velocity of the monolayer. It can be shown, however, that the expansion speed does not depend on the average cycle time alone, but also on the cycle time distribution which is not considered in this measure. For a Γ-like, non-Poissonian cycle time distribution the growth rate of the population in the exponential regime and the expansion velocity of the radius is the smaller the sharper the cycle time is peaked [12,37]. For example, the growth rate of the radius of gyration in Fig. 3b is not $(1/2)(1/\tau)$, but $(1/2)(ln(2)/\tau)$ (the factor $(1/2)$ enters by the space dimension "2"). It can be calculated explicitly if the cycle-time distribution can be
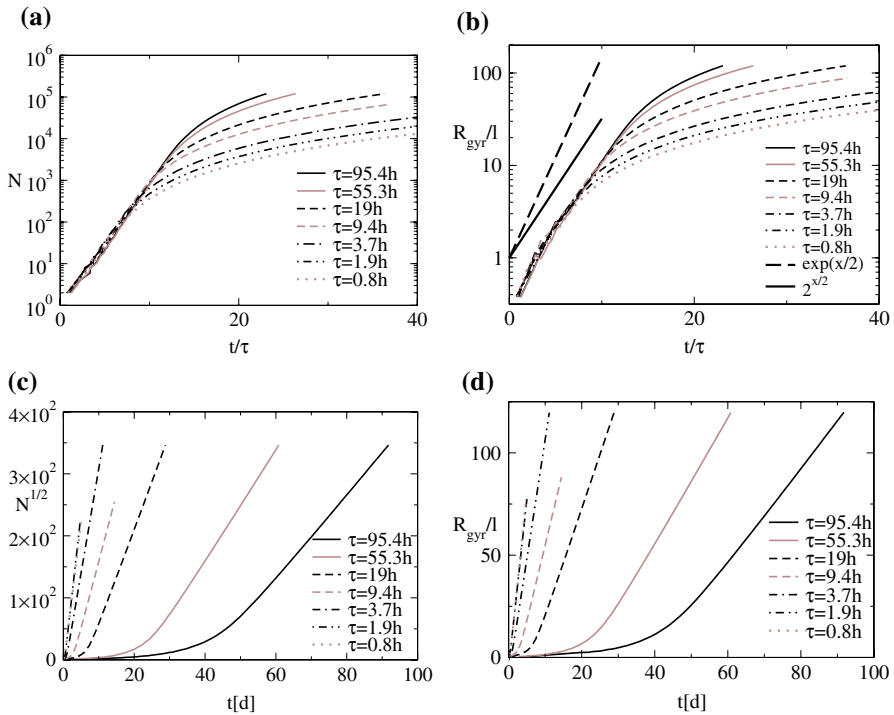
Fig. 3 **a** The population size $N(t)$ grows initially exponentially fast. **b** The corresponding curves for the radius of gyration also shows exponential growth. **c** For long times, $N^{1/2} \propto t \Leftrightarrow N \propto t^2$, and **d** $R_{gyr} \propto t$. All figures show growth curves for different cycle length durations. The growth velocity for long times can be obtained from $v = dR/dt$ using that for circular dense monolayers $R = \sqrt{2}R_{gyr}$ (see Fig. 6). (Results obtained by simulations with the individual-based off-lattice model.)

approximated by an Erlang-distribution ([12,34]; in this case $\tau_{\text{eff}} = \beta\tau$ with $\beta > 1$; see Sect. 3.1). In the remaining of this section we do usually not distinguish between τ and τ_{eff}. The former has to be used for a Poissonian cycle time distribution while for a sharply peaked Erlang(-like) distribution, τ has to be replaced by τ_{eff} (Fig. 4).

The measure $v \approx \Delta L/\tau$ does not give any information of how sharp the interface between proliferating and non-proliferating (quiescent or necrotic) cells in the monolayer is. Moreover, the measure requires long-time simulations to large cell population sizes to insure that the growth is sufficiently far in the asymptotic, linear growth regime where $v = $ const. to eliminate possible cross-over effects from the exponential to the linear growth regime which otherwise could disturb the determination of the asymptotic growth velocity. Therefore we also use a different definition of the width of the proliferating rim by labelling all those cells which did not undergo a cell division for a time period of at least $\Delta t_{\text{th}} = 2.5\tau$ (Fig. 5). The layer thickness then is defined by

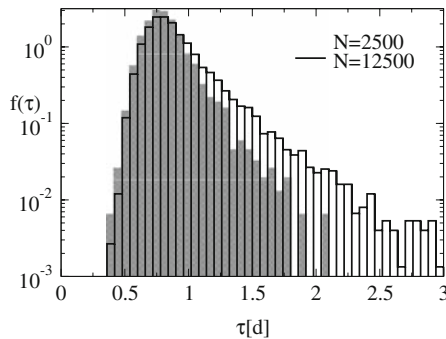$$\Delta L = \sqrt{2}\left(R_{gyr}^{(N)} - R_{gyr}^{(N_r)}\right). \tag{5}$$

Fig. 4 Cycle time distribution of cells at the $N = 2,500$ (*grey*) and $N = 12,500$ (*black lines*) cells stage, respectively. The cycle time distribution is peaked and resembles a Γ-distribution. The average cycle time is $\tau \approx 0.82\,\text{day} = 19.5\,\text{h}$ for $N = 2,500$ cells and $\tau \approx 0.9\,\text{day} = 21.6\,\text{h}$ for $N = 12,500$ cells. The elongation of the cycle time is the consequence of the mechanical cell deformation for cells in mechanical contact. For $N = 2,500$ cells almost all cells behave as if they were isolated, hence the growth is exponentially fast and the cycle time distribution is as those almost that for isolated cells. For $N = 12,500$ cells, however, a considerable fraction of the cells is inhibited from growth and division by contact inhibition, so those cells at the inner border of the proliferating rim have a longer than expected cycle time. (Results obtained by simulations with the individual-based off-lattice model.)

Here, $R_{gyr}^{(N)}$ is calculated from the total cell population size N while $R_{gyr}^{(N_r)}$ is calculated from the N_r cells which did not divide during the period of time Δt_{th}. This quantity has a much shorter cross-over behaviour between the initial exponential and the asymptotic linear growth regime and hence leads to a stable value for ΔL at smaller population sizes. However, the numerical value for the threshold Δt_{th} is to some extent arbitrary, and should be chosen such that only a negligible fraction of cells in the exponential growth regime are found to overcome this threshold. We used both values to test our qualitative predictions on how v and ΔL depend on the growth rate $1/\tau$. By variation of the intrinsic cycle time τ (the cycle time of a cell in the absence of any cell–cell interactions; see Appendix A for details), we obtain for the velocity of the monolayer expansion:

$$v = \frac{dR}{dt} = c_1 \frac{1}{\sqrt{\tau}} \tag{6}$$

and consequently for the thickness ΔL of the proliferating rim:

$$\Delta L = c_2 \sqrt{\tau}, \tag{7}$$

since $v = \Delta L/\tau \propto 1/\sqrt{\tau}$. The proportionality constant c_1 depends on other factors such as the sensitivity towards contact inhibition (d_c) and the biomechanical parameters of the cell. The constant c_2 furthermore depends on the definition of the thickness of the proliferating rim. From Fig. 6a one obtains $c_1 = 13.3\,\mu\text{m}/\sqrt{\text{h}}$ and, using $v = \frac{dR}{dt} = c_1 \frac{1}{\sqrt{\tau}} = \Delta L/\tau_{\text{eff}}$, one obtains $c_2 = c_1/\ln(2) \approx 19\,\mu\text{m}/\text{h}^{1/2}$. For example, if $\tau = 19\,\text{h}$ as for rat astrocytes, this yields a proliferating rim thickness of $\Delta L = 82\,\mu\text{m}$ (the cell size of rat astrocytes is $l \approx 10\,\mu\text{m}$ [37]). Comparison with
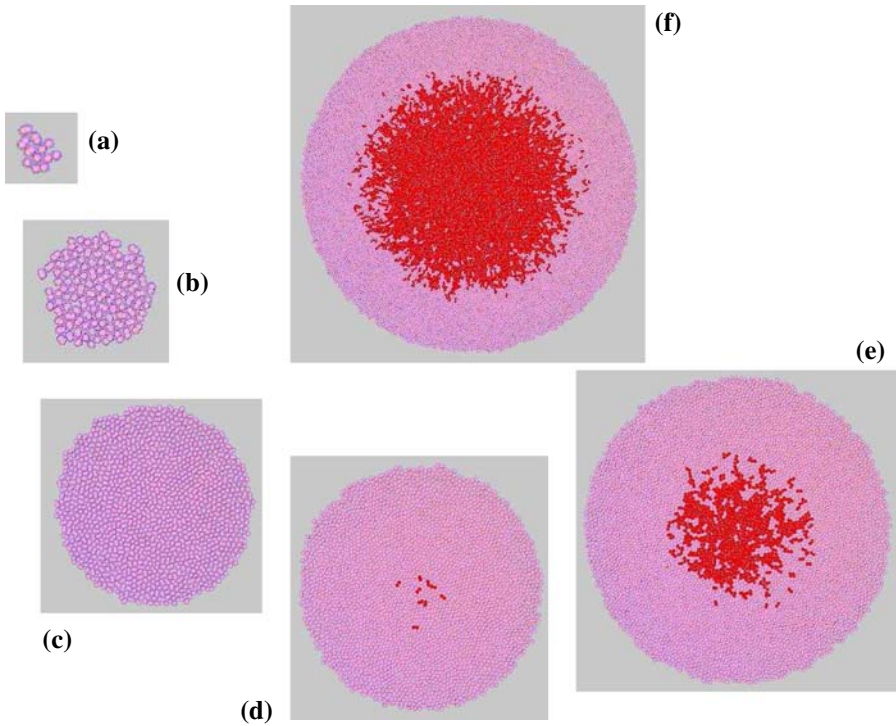
Fig. 5 Typical growth scenario of dense monolayers. The red cells did not divide for a period of time of $\Delta t > 2.5\tau = \tau_{th}$ while for the pink cells, $\Delta t \leq \tau_{th}$. The layer thickness was defined by Eq. 5. where N_r denote the *red* cell population, N the total cell population. **a** $N = 10$, **b** $N = 100$, **c** $N = 1,000$, **d** $N = 2,500$, **e** $N = 5,000$, **f** $N = 12,500$. (Results obtained by simulations with the individual-based off-lattice model.)
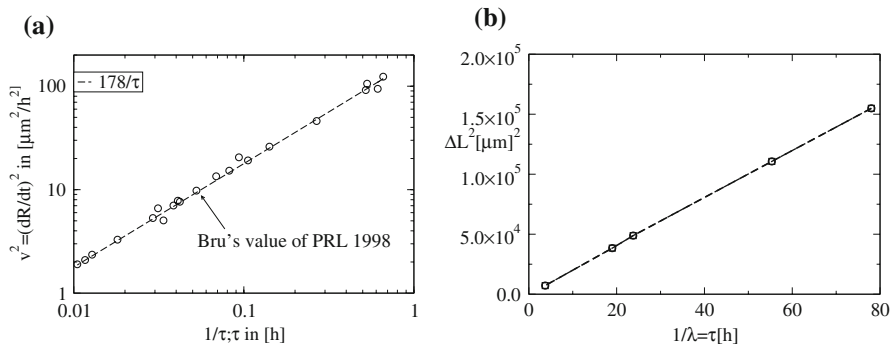

Fig. 6 **a** Square of spreading velocity v^2 of a monolayer versus $1/\sqrt{\tau}$ in a log–log plot. The *arrow* denotes the value in Ref. [15] to indicate that the range presented in this figure corresponds to realistic monolayer spread velocities. In a subsequent publication, Bru et al. [14] reported values from 1 to 11 μm. **b** Thickness of the proliferating rim versus τ for five representative values selected from **a**. (Results obtained by simulations with the individual-based off-lattice model. *Lines* represent least-mean-square fits.)

the pressure profiles in Fig. 7h shows that the value of $\Delta L = 82\,\mu$m is in agreement with the range over which the pressure decays from p_0 to its minimum value. From Fig. 6b where ΔL was defined using Eq. 5 we obtain $c_2 = 44\,\mu$m/h$^{1/2}$ instead. Hence, Fig. 5f, where cells with a cycle time duration of $\tau < \Delta t_{\text{th}} = 2.5\tau$ are marked in pink, overestimates the thickness of the layer by a factor of two. Comparing to Fig. 7d (in Fig. 7 the same parameter values as for Fig. 5 have been used) shows, that only cells for which the true cycle time was approximately $\leq \tau = 19$ h (those are marked in white) contribute to the expansion of the monolayer.

A continuum model for compact monolayers must guarantee the integrity of the monolayer and should reproduce the following features:

(1) the initial exponential and the large-scale linear expansion of the monolayer diameter. Note, that in the reaction diffusion model of the sparse monolayer cultures, the initial spread is not exponentially fast.
(2) Furthermore, the velocity in the linear expansion regime should grow with $v \propto 1/\sqrt{\tau} = \sqrt{s_0}$ where s_0 denotes the growth rate. The thickness of the variable rim then is $\Delta L = c_2\sqrt{\tau}$.

2.2 The continuum model for compact cell aggregates

In this section we use the insight gained from the agent-based model to derive a continuum model that is similar in form to existing mechanical models of solid tumour growth originally proposed by Greenspan [46]. For consistency with the agent-based simulations, we require that the governing equations incorporate the following key properties:

– Cell growth and division are controlled by a biomechanical form of contact inhibition; as long as no cell within an aggregate has overcome the critical threshold for contact inhibition, growth is exponentially fast. The critical threshold is determined by the compression that a cell experiences (see model assumption A5). However, by Eq. 3 we can assign to the critical compression a critical pressure (see also model assumption A5). In Fig. 7b we show the results of a measure for the pressure in our computer simulations. We defined the pressure on cell i by

$$p_i = \sum_{j \, nn \, i} \frac{F_{ij}^{rep}}{A_{ij}}, \tag{8}$$

where F_{ij}^{rep} denotes the (JKR-) force between the nearest spheres of the dumbbells i and j in the absence of cell–cell adhesion, A_{ij} the corresponding contact area. The sum is conducted over all cells j with are exerting a force on cell i. A similar relation has been used in Ref. [67] to investigate the pressure on a cell. We use this simple definition since within our model we cannot directly calculate the volume of the cells so cannot strictly distinguish between cell compression and deformation forces and stresses. Moreover, we cannot directly calculate the precise
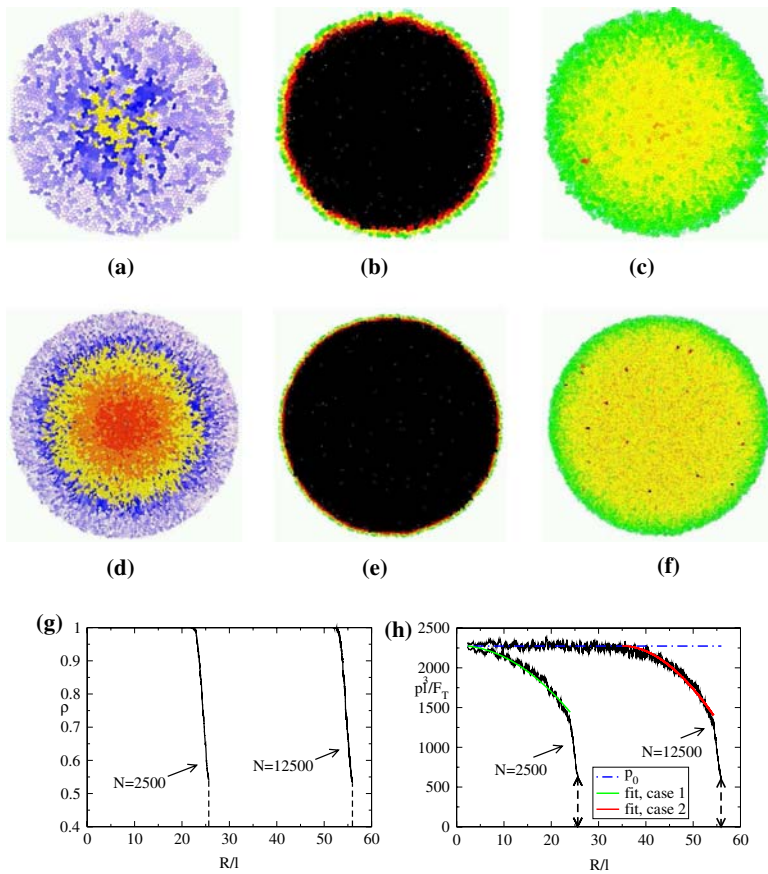
Fig. 7 **a** Cell division frequency, **b** space filling fraction, **c** pressure of cells in a dense monolayer at the $N = 2,500$ cells stage and **d** cell division frequency, **e** space filling fraction, **f** pressure of cells in a dense monolayer at the $N = 12,500$ cells stage. **g** Comparison of cell space filling $\varrho(R/l)$-and **f** the pressure profile $p(R/l)$ for $N = 2,500$ and $N = 12,500$ cells. We used the space filling fraction ϱ to determine the distribution of cells in space since this quantity is smoother than the density n (cf. [40]). In **a–f** the intensity scales linear with the values: **a, d** *white* cells for which the last cell division occurred $< 2\tau$, *blue* $< 4\tau$, *green* $< 6\tau$, *orange* $< 8\tau$ and red $< 10\tau$. **b, e** *black* space filling $n/n^* = 1$ while decrease is linear from *black, red, green, yellow* ($n/n^* = 0.43$); **c, f** *red*: $p \approx 2250$–2500 (in units of F_T/l^3), *yellow*: $2250 > p > 1950$, *green*: $p \leq \sim1950$. While the division frequency and the pressure pattern both decay smoothly in a boundary region (compare **a** to **c**), the density shows a sharp decay at the monolayer border. By comparison with Fig. 4 only cells with $\tau' \leq \Delta t \approx 2.5\tau$ divide, i.e., the *white* cells in **a** and *green* cells in **c**. **g** Shows that the space filling fraction ϱ is almost one over the whole monolayer and sharply decays at the monolayer border. **h** In contrast to ϱ, the pressure p decays slowly from its maximum value $p^0 \approx 2,280$ (in units of l^3/F_T, dashed line) to $p = 0$ at the border. The vertical jump at the front of the profile results from the pressure contribution by cell–cell adhesion. For $N = 2,500$ cells p_0 is nowhere reached in agreement with the proliferation profile **a** (see also Fig. 5d) and the observation of exponentially fast cell division at $N \approx 2,500$ cells (Fig. 3a). Sub-figures **a–f** and the *black curves* in **g, h** are results obtained by simulations with the individual-based off-lattice model. The *green* and *red curve* denote fits to the pressure profiles given by Eqs. 17 and 20, respectively. From the fits we find $R_p \approx 35l \approx 350\,\mu$m for cells with diameter $l = 10\,\mu$m, $\gamma \approx 0.03$ N/m (surface tension) and $\mu \approx 1.5 \times 10^{-14}$ m^{3}s/kg (quotient of permeability and viscosity). (Compare **g, h** to the results of the continuum model in Sect. 2.2 where the coordinate R/l is denoted by r.)

shape of a cell that interacts with other cells. However, our measure represents the total pressure needed to compress a previously uncompressed cell to the observed compression. Usually a cell can escape pressure exerted from one side only, so a compression from one side of the cell alone is usually insufficient to overcome the critical threshold necessary for a stop of proliferation. Instead a cell i has to be squeezed between other (usually about 6) neighbour cells j each up to p_0^{ij} (see A5) in order to stop proliferating. In the presence of cell–cell adhesion cells are compressed or deformed as a consequence of the adhesion force between neighbouring cells while in the absence of cell–cell adhesion cell compression can only occur as a consequence of external forces. The adhesion between neighbouring cells leads to a compression which is given by the distance at which the cell–cell interaction potential energy V_{ij} has its minimum. Hence the above definition of p_i includes the pressure due to cell–cell adhesion. An alternative measure of pressure would involve the JKR force (including the adhesive contribution). However, then in this case the critical compression needed to reach the critical threshold p_0 would depend on the kind of stimulus responsible for the pressure on a cell i. (For the simulated cell populations studied here, this would only lead to an approximately constant negative shift of the force curve and would not affect our results).

On the other hand, Fig. 7c shows that the filling fraction ϱ, i.e., the space filled by cell mass is almost at its saturation value indicating the density is constant apart from the border of the monolayer (Fig. 7a).

– Once the critical threshold for contact inhibition is exceeded in the interior of the monolayer, growth becomes localised to a layer at the surface of the multi-cellular aggregate. Hence, above a certain threshold for the local mechanical stress, contact inhibition prevents cell division from occurring within the aggregate (Fig. 7e). Again, $\varrho \approx 1$.
– Nutrients are not growth-rate limiting.

At the continuum level, the above assumptions are embodied in a mass balance equation (Eq. 9), a momentum balance equation (Eq. 10) and a constitutive law. Here we consider

$$\frac{\partial n}{\partial t} + \nabla.(n\underline{v}) = f(p_0 - p) \tag{9}$$

$$\underline{v} = -\mu\nabla p. \tag{10}$$

In Eqs. 9 and 10 $n = n(\underline{r}, t)$ is the local cell density, $\underline{v} = \underline{v}(\underline{r}, t)$ the local velocity, $p(\underline{r}, t)$ the (cell) pressure and $f(p_0 - p)$ a source term representing cell division. Following [46] we use Darcy's law (10) to describe the tendency of cells to move down pressure gradients and away from regions of high mechanical stress (see Eq. 12). Darcy's law was originally used to describe fluid flow through a porous medium and can be derived using homogenisation techniques from the Stokes equation (i.e., the Navier–Stokes equation in the limit of negligible inertia).

Equations 9 and 10 do not define a closed system for n, $\underline{v}$ and p: an additional constitutive assumption is needed. Usually, this system of equations needs to be closed by a constitutive equation $p(n)$. Guided by Fig. 7b we assume that the cell density $n \propto \varrho$ is constant and at its saturation value $\varrho^* \approx 1$ throughout the monolayer.

Additionally, direct comparison of Fig. 7a and c ($N = 2, 500$ cells) and Fig. 7d and f ($N = 12, 500$) suggest that cell proliferation is localised in regions where the local pressure is below the threshold p_0. Under these assumptions Eqs. 9 and 10 simplify to give the following, closed system of equations:

$$\nabla \cdot \underline{v} = s_0 H(p_0 - p), \tag{11}$$

$$\underline{v} = -\mu \nabla p, \tag{12}$$

where $H(p_0 - p)$ denotes the Heaviside step function:

$$H(x) = \begin{cases} 1 & \text{if } x > 0, \\ 0 & \text{otherwise.} \end{cases} \tag{13}$$

With $n \approx 1$, the mass balance equation (see Eq. 11) relates the cell velocity $\underline{v}$ to the local growth rate $s_0 \propto 1/\tau$ and the threshold pressure p_0 above which growth and proliferation are contact-inhibited. Similar models have been studied by many other authors including Cristini et al. [28]. However, the earlier works focus on nutrient-limited rather than stress-regulated growth. We remark that the JKR-force does not appear explicitly in Eqs. 9–12. For growth in compact monolayers the precise form of the interaction force is not important (see [38]): all that is needed is a sufficiently strong adhesion force: compactness of the monolayer is guaranteed by the assumption $n \approx 1$.

Guided by the numerical simulations for the agent-based model (see Fig. 5), we assume that the aggregate grows as a radially symmetric circular mass. The position of the outer boundary of the expanding aggregate is denoted by $r = R(t)$ and is assumed to move with the cell velocity there so that

$$\frac{\partial R}{\partial t} = \underline{v}.\hat{n}\big|_{r=R}, \tag{14}$$

where $\hat{n}$ is a unit normal to the surface of the cellular aggregate which, for radially symmetric growth, points in the outward radial direction. When growth is one-dimensional, Eqs. 11 and 12 can be combined to eliminate $\underline{v} = (v(r, t), 0, 0)$, giving

$$-\frac{\mu}{r} \frac{\partial}{\partial r} \left(r \frac{\partial p}{\partial r} \right) = s_0 H(p_0 - p). \tag{15}$$

The governing equations are closed by imposing the following boundary and initial conditions:

$$\frac{\partial p}{\partial r}\bigg|_{r=0} = 0, \quad p|_{r=R} = \frac{\gamma}{R}, \quad R(t = 0) = R_0. \tag{16}$$

The first boundary condition guarantees symmetry of the aggregate about $r = 0$ while the second balances the pressure jump across $r = R(t)$ with surface tension. Here, we assume, that the pressure outside the aggregate is zero taking into account that the

situation we model are monolayers on a flat substrate or in liquid medium. γ mimics the surface tension of the multi-cellular aggregate which in the single-cell-based model emerges as a consequence of cell–cell adhesion, thus favouring monolayer aggregates that are circular. The macroscopic surface tension emerges from the (microscopic) cell–cell adhesion and depends on the form of the cell–cell interaction (JRK-model in this paper, extended Hertz model in Ref. [38]). However, in order to monitor this dependency explicitly, a rigorous coarse graining procedure would be necessary which is currently too involved for the single-cell-based off-lattice model.

We remark that the continuum model defined by Eqs. 11–16 is similar to models developed by other authors including Greenspan [46], Byrne and Chaplain [18]. An important and distinguishing feature of the present model is the dependence of the proliferation rate on the cell pressure p: in most existing models, nutrient availability controls the tumour's growth rate. When constructing solutions to the continuum model, we consider separately cases for which all cells within the aggregate proliferate freely and cases for which contact inhibition prevents cells towards the centre of the cluster from dividing.

Case 1. In this case $p_0 > p$ throughout the aggregate and integration of (Eq. 15) subject to the boundary conditions (Eq. 16) yields:

$$p(r, t) = \frac{\gamma}{R} + \frac{s_0}{4\mu} \left(R^2 - r^2 \right). \tag{17}$$

In particular, the maximum pressure occurs at the aggregate centre, $r = 0$, in agreement with simulations of the single-cell-based model. Inserting Eq. 17 into Eq. 12, and the result in Eq. 14 integrating with respect to time yields

$$R(t) = R(t = 0)\, e^{s_0 t/2}. \tag{18}$$

Further, for 2D circular growth, $N(t) = \pi R^2 \propto e^{s_0 t}$, in agreement with the simulations of the single-cell-based model. This exponential growth phase persists until p passes through p_0 and contact inhibition prevents cells from proliferating. We assume that this transition occurs when $R = R_{cr}$. Using (Eq. 17) and noting that if $R = R_{cr}$ then $p = p_0$ at $r = 0$ and $p < p_0 \; \forall \, r \in (0, R_{cr})$, we may derive the following algebraic expression for the critical radius R_{cr}:

$$0 = R_{cr}^3 - \frac{4\mu p_0}{s_0} R_{cr} + \frac{4\mu\gamma}{s_0}. \tag{19}$$

We note that if $\gamma = 0$ (i.e., if surface tension effects are negligible) then $R_{cr} = 2\sqrt{\mu p_0/s_0}$. Otherwise, if $\gamma > 0$ then (19) has two positive roots $0 < R_{cr,1} < R_{cr,2} < 2\sqrt{\mu p_0/s_0}$. The smaller root $R_{cr,1}$ defines the size of the smallest aggregate for which valid solutions exist (it can be viewed as a nucleation radius): if $R < R_{cr,1}$ then surface tension effects dominate and $p \geq p_0$ at $r = 0$. It is also possible to show that the physically relevant root, $R = R_{cr,2}$, decreases as γ increases, i.e., surface tension effects caused by stronger cell–cell adhesion reduce the aggregate size at which contact

inhibition becomes important, a result which is also in agreement with predictions of the agent-based models.

Case 2. The cluster now possesses a central core ($0 < r < R_p(t)$) in which cells are contact-inhibited from proliferating. Since p and $\frac{\partial p}{\partial r}$ are continuous across $r = R_p$ then integration of (Eq. 15) subject to (Eq. 16) yields:

$$p(r,t) = \begin{cases} p_0, & \text{for } 0 < r < R_p(t), \\ p_0 - \frac{s_0 R_p^2}{2\mu} \ln\left(\frac{R_p}{r}\right) - \frac{s_0}{4\mu}\left(r^2 - R_p^2\right), & \text{for } R_p(t) < r < R(t). \end{cases} \tag{20}$$

In (20) we determine $R_p(t)$ implicitly in terms of R and system parameters by imposing $p = \gamma/R$ on $r = R$, giving:

$$\frac{\gamma}{R} = p_0 - \frac{s_0 R_p^2}{2\mu} \ln\left(\frac{R_p}{R}\right) - \frac{s_0}{4\mu}(R^2 - R_p^2). \tag{21}$$

The evolution of $R(t)$ is determined by substituting with p from Eq. 20 into Eq. 12, and the result into Eq. 14:

$$\frac{dR}{dt} = -\mu \left.\frac{\partial p}{\partial r}\right|_{r=R} = \frac{s_0}{2R}(R^2 - R_p^2). \tag{22}$$

In summary, Eqs. 21 and 22 characterise the evolution of the aggregate when $R > R_{cr}$.

In order to make analytical progress and highlight further the link with the individual-based model, we focus on the long-time behaviour, introducing a small parameter $0 < \epsilon \ll 1$ and rescaling the independent and dependent variables as follows:

$$R(t) = \frac{\bar{R}(\hat{t})}{\epsilon}, \quad R_p(t) = \frac{\bar{R}(\hat{t})}{\epsilon} - R_{p1}(\hat{t}) + \epsilon R_{p2}(\hat{t}), \quad t = \frac{\hat{t}}{\epsilon}.$$

By substituting with these approximations in Eqs. 21–22 and equating to zero coefficients of $O(\epsilon^n)$ we deduce

$$\bar{R}(\hat{t}) = R^* + 2\sqrt{\mu s_0 p_0}\hat{t}, \quad R_{p1}(\hat{t}) = 2\sqrt{\frac{\mu p_0}{s_0}}, \text{ constant,}$$

where R^* is a constant and $s_0 \propto 1/\tau$. Thus, at long times the outer radius of the aggregate grows linearly with time and the width of the proliferating rim is constant. Additionally, the pressure in the central core remains constant.

These results are in good agreement with computer simulations presented in Fig. 7h. Moreover, we used Eqs. 17 and 20 for a fit of the pressure profiles in Fig. 7h for the exponential growth phase (case 1) and the linear expansion phase (case 2), respectively. The found fit parameters are $R_p = 350\,\mu$m, the pressure threshold is $p_0 \approx 228\,$N/m^2, the tissue surface tension of $\gamma = 0.03\,$N/m which is within the range of values found for tissue cell aggregates in Ref. [11], and an effective value for the ratio of the permeability

and viscosity of $\mu \approx 10^{-14} \text{m}^3 \text{s/kg}$. Typical tissue viscosities are about $\sim 10^5$ Pa s [11] from which an effective permeability of $\sim 10^{-9} \text{m}^2 \approx 10 \, \mu\text{m}^2$ is obtained, which is of the order of the cross sectional area of a cell. Hence, the comparison of simulation results with the single-cell based model with the analysis of the continuum mechanical model, although both models are certainly oversimplified, permit to estimate the model parameters in the continuum model. Note, that cells in the interior of the monolayer may re-arrange their cytoskeleton to locally relax the stress [38]. This, however, does not affect the cells in the proliferating rim.

3 Sparse phenotype (type II)

3.1 Agent-based models: lattice-free and cellular automaton model

Lattice-free agent-based model In principle, type II monolayers may be studied using the same (lattice-free) agent-based model as used above for type I monolayers. Figure 8 shows a typical growth scenario with zero cell–cell adhesion ($\varrho_m = 0$) and otherwise the same parameters as in Fig. 5. Different from type I monolayers the cells are initially sparsely distributed in space (Fig. 8a, b) before they form a dense loose lump of cells that—other than for type I monolayers—is not stabilised by cell–cell adhesion.

Figure 9 shows the corresponding growth curves until $N = 12,500$ cells together with the corresponding curves in the presence of adhesion (type I-monolayers) and the curves for pure hard core repulsive interaction for comparison. The growth scenario for the population size for type II monolayers is the same as for type I monolayers (Fig. 9a).

However, the initial growth of the radius of gyration shows a characteristic bump reflecting the lack of cell–cell adhesion.

Simulations with varying growth rates suggests the same qualitative relation $v = \hat{c}_1 \sqrt{1/\tau}$ as for type I—monolayers (Fig. 10). However, if cell–cell adhesion is lacking, cells can freely migrate which leads to a larger growth velocity than in the presence of cell–cell adhesion. Consequently, $\hat{c}_1 > c_1$ (compare Figs. 6a, 10). Consistently with this observation the thickness of the layer, in Fig. 9 again denoted by the pink cells for which $\tau < \Delta t_{\text{th}} = 2.5$, is larger without than in the presence of cell–cell adhesion (compare Fig. 9). Again the velocity may be used to calculate the width of the proliferating rim. However, in the absence of cell–cell adhesion some cells detach from the main central aggregate and migrate away. Hence, the value obtained for the width of the proliferating rim using

$$v = dR/dt = \hat{c}_1/\sqrt{\tau} = \Delta L_{\text{eff}}/\tau_{\text{eff}} \tag{23}$$

now is an "effective" quantity since it includes both those cells that were pushed aside by other proliferating cells and those which migrate freely after detaching from the central aggregate. When cell–cell adhesion is sufficiently strong, and cell detachment cannot occur, ΔL is determine solely by cells that are in contact with the central monolayer aggregate. This aspect will be discussed in more detail below.
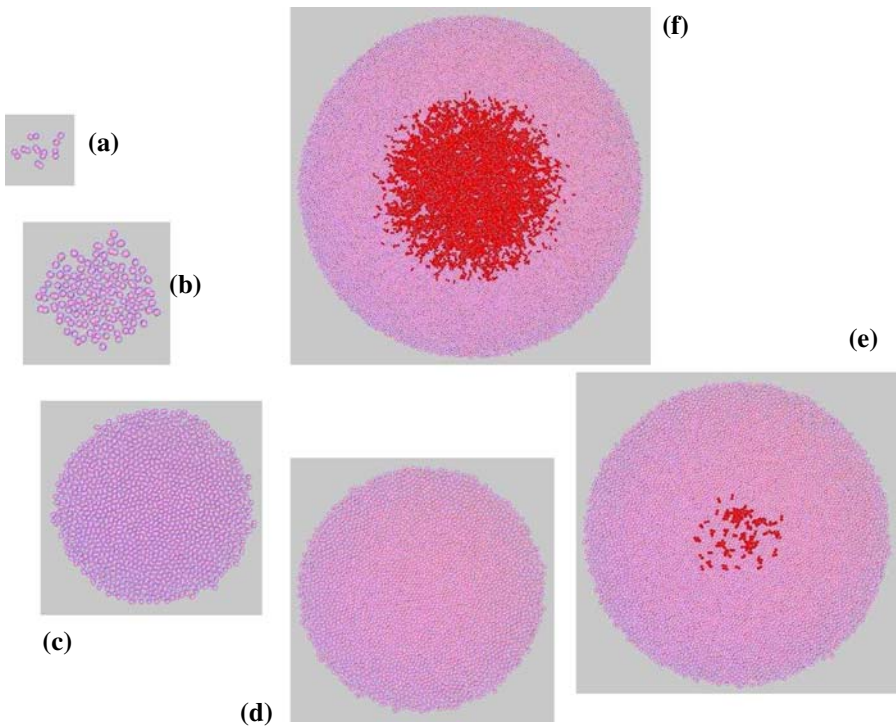
Fig. 8 Typical growth scenario in the absence of cell–cell adhesion. The red cells did not divide for a period of time of $\Delta t > 2.5\tau = \tau_{th}$ while for the pink cells, $\Delta t \leq \tau_{th}$. The layer thickness was defined by Eq. 5. where N_r denote the red cell population, N the total cell population. **a** $N = 10$, **b** $N = 100$, **c** $N = 1,000$, **d** $N = 2,500$, **e** $N = 5,000$, **f** $N = 12,500$. Note, that for small sizes the cell population does not form a compact aggregate but form a sparse distribution. The formation of a central region of non-proliferating cells occurs later than in the presence of cell–cell adhesion and after it has formed, the central region is smaller (compare Fig. 5). Vice versa, the size of the proliferating rim is larger resulting in a larger growth speed of the monolayer for long times. Note, however, that here the *pink* layer include those cells in contact to the main central cell aggregate and those which have detached from the central aggregate and migrated away. (Results obtained by simulations with the individual-based off-lattice model.)

Note, however, that the cell aggregates in absence of cell–cell adhesion are still circular in shape i.e., no buckling or fingering occurs (Fig. 8). This can change if cell aggregates grow in an environment of other cells or granular matter instead of liquid medium (e.g. [38,42]) or if the growth is nutrient-limited.

A systematic analysis of the initial growth of the radius of gyration requires computer simulations at very large migration activities (large D) or at very long cycle times. For these cases simulation times using the lattice-free agent-based model become too large to be practical. This was the motivation for proposing a cellular automaton model that was parameterised in such a way that the system behaviour of type I and type II monolayers could systematically be explored [12]. However, it is important to notice that cellular automaton models are largely rule based while in the lattice-free agent based model the physical interactions are directly represented. This may limit the predictive power of CA-simulations and facilitate to overlook certain
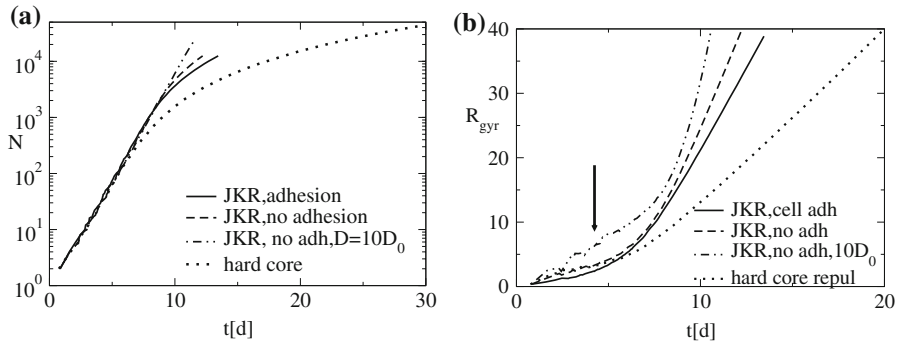
(a)

(b)

Fig. 9 Cell kinetics for type II monolayers. **a** Population size vs. time in a semi-log plot, **b** radius of gyration versus time. Note the bump for small times in (*arrow* in **b**). The simulation for pure hard core repulsion (i.e., no Hertz-interaction) has been added to demonstrate, that the repulsive Hertz-interaction elongates the initial exponential growth phase (**a**) and increases the speed of expansion of R_{gyr} for long times (**b**). (Results obtained by simulations with the individual-based off-lattice model. Further details, see text.)

Fig. 10 Square of spreading velocity v^2 of a monolayer versus $1/\sqrt{\tau}$ in a log–log plot for type II monolayers. (Results obtained by simulations with the individual-based off-lattice model.)
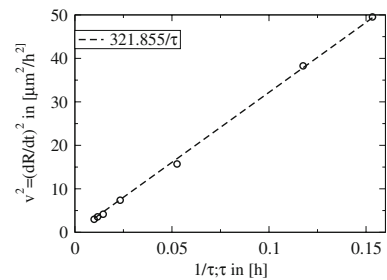
biological phenomena. For example, the transition from type I to type III monolayers that occurs in the absence of growth control mechanisms can easily be overlooked within a cellular automaton model since compression effects on length scales below the cell diameter are difficult to represent. One the other hand, cellular automaton approaches have important advantages: the simulations are about 1,000-times faster than those with lattice-free agent based models, hence ensemble averages over many realisations of stochastic multicellular growth processes are possible and population sizes of $O(10^7 - 10^8)$ cells are amenable, more than one order of magnitude more than those amenable by off-lattice simulations at the moment.

In Ref. [12] we carefully analysed how the parameters within the cellular automaton model have to be chosen to obtain the same growth kinetics as for the lattice-free agent based model.

For sparse monolayers it is possible to obtain a continuum equation by a systematic derivation based on methods from statistical field theory [34]. By comparison with the systematic analysis of the cellular automaton model it is possible to extend the continuum equation to capture most of the system behaviour of growing monolayers for parameter combinations for which a systematic derivation is not possible so far.

We firstly summarise the rules of the cellular automaton approach introduced in Ref. [12] and then explain how the above analysis of type I monolayers help to identify hidden parameter dependencies. The cellular automaton approach is suited to model type I and type II monolayers. Then, we use the same parameter dependencies to extend the limiting continuum equation.

The cellular automaton model: The cellular automaton model is defined by the following rules [12]:

R1: Each lattice site can be occupied by at most one single cell.
R2: A dividing cell is able to push aside at most $\Delta L/l - 1 \geq 0$ neighbour cells. We pursue this by assuming that a cell can divide if and only if there is at least one free neighbour site within a circle of radius ΔL around the dividing cell.
R3: When a cell divides, one of its daughter cells is placed at the original position of the mother cell. Then the closest free lattice site within a circle of radius ΔL is searched and a line connecting the closed free lattice site and the site of the mother cell is drawn. The second daughter cell is placed on that neighbour lattice site of the first daughter cell that is closest to the line. All other cells are arranged along the line such that then closes free lattice site is now occupied by a cell.
R4: The (intrinsic) cell cycle time τ' is distributed according to an Erlang-distribution, the discrete analog to the Γ-distribution, i.e.,

$$f(\tau') = \lambda_m \frac{(\lambda_m \tau')^{m-1}}{(m-1)!} \exp\{-\lambda_m \tau'\} \tag{24}$$

with $\lambda_m = m$ such that $\langle \tau' \rangle = \tau = 1$. For $m = 1$, $f(\tau)$ is Poisson-distributed. For $m \to \infty$, $f(\tau')$ approaches a δ-distribution, peaked at $\tau' = \tau$. For intermediate m the shape is as in Fig. 4.
R5: A cell hops with rate ϕ to a free neighbour site irrespective of the number of neighbour cells before and after its hop. This rule corresponds to free random cell migration which in the lattice-free model occurred in the limit of no cell–cell adhesion. For $\phi = 0$ no random cell migration occurs.

(A detailed explanations of the model assumptions can be found in Ref. [12].) The model parameters are hence the expected cycle time τ, the parameter m that controls the shape of the cycle time distribution, the parameter ϕ, that determines the diffusion constant of isolated cells, and the pushing parameter ΔL that emerges from the threshold for contact inhibition in the lattice-free agent-based model.

The simulations show the same growth scenarios as the lattice-free agent-based model but permit to choose ϕ very large which corresponds to a large cell diffusion constant $D = l^2 \phi/2d$ ($d = 2$ is the spatial dimension [12]). For short times, $N \sim e^{t/\tau_{\text{eff}}}$ and $R_{gyr} = \sqrt{(\phi + 1/\tau_{\text{eff}})t}$ where $\tau_{\text{eff}}^{-1} = (2^{1/m} - 1)m\tau^{-1}$ is the effective growth rate. For long times $\sqrt{2d}R_{gyr}/dt = v = \text{const}$ and $N \propto t^2$ with [12]:

$$v^2 \propto \left([f(\Delta L)]^2/\tau_{\text{eff}} + l^2 \phi\right)/\tau_{\text{eff}}. \tag{25}$$

$f(\Delta L)$ is a linear function of ΔL. Its precise form depends on the lattice type and update rules [12]. In the CA-model, ΔL is an independent parameter that does not emerge from the cell properties. However, both, the agent-based lattice-free model and the continuum mechanical models both show that ΔL is not independent of the other parameters, but does depend on the cycle time duration by Eq. 7. Hence, if the cycle time is modified, the parameter ΔL must be modified according to $\Delta L \propto \sqrt{\tau}$. This is crucial to use the cellular automaton model to predict the behaviour of monolayers for different cycle times if cell division is controlled by the biomechanical form of contact inhibition introduced above. As in Eq. 23 one can define an effective width of the layer by $v = \Delta L_{\mathrm{eff}}/\tau_{\mathrm{eff}}$ with v from Eq. 25. Only if no free diffusion of cells occurs, i.e., if $D \propto \phi = 0$, $\Delta L_{\mathrm{eff}} = f(\Delta L)$. Otherwise the proliferative rim consists of cells that move due to pushing (these are characterised by ΔL) and those that detach from the main aggregate by free migration. The second contribution can be estimated from the second term on the rhs. of Eq. 25 using $\Delta L_{\mathrm{eff}} = \hat{c}_1/ln(2.)\sqrt{\tau} = \left[f(\Delta L)^2 + l^2\phi\tau_{\mathrm{eff}} \right]^{1/2}$.

3.2 Continuum model

For large migration rates in the absence of cell–cell adhesion the growing cell aggregate does not have such a sharp interface with the embedding medium as in the case of type I monolayers (Figs. 5, 8). Hence one can assume that for this case the cells are locally sufficiently homogeneously and isotropically distributed on scales larger than the cell diameter but smaller than the linear dimension of the multi-cellular aggregate. In this case, the dynamics of the cell configuration can be modelled by a multivariate (population) master equation [34]. This equation can be used to derive an approximate stochastic continuum equation of the reaction-diffusion type, a stochastic form of the FKPP-equation:

$$\frac{\partial n(\underline{r}, t)}{\partial t} = D\Delta n(\underline{r}, t) + (s_0 - d_0)n(\underline{r}, t)(n^* - n(\underline{r}, t)) + \sqrt{2s_0 n(\underline{r}, t)}\eta. \quad (26)$$

Here, $n(\underline{r}, t)$ is the local cell density, s_0 the growth rate, d_0 the death rate, η Gaussian white noise with zero mean and variance 1, $D = l^2\phi/2d$ (here: $d = 2$) the diffusion constant. n^* is the local cell saturation density. It is known that for long times the equation shows a travelling wave behaviour for initial conditions $n(r, 0) = n^*$ for $r < r_0$ (r here is the radius in polar coordinates) and $n(r, 0) = 0$ otherwise. If the noise term is neglected one obtains the classical FKPP-equation. In order to capture the effect of division on the travelling front we proposed to replace D by an effective diffusion constant D_{eff} defined by

$$D_{\mathrm{eff}} = [f(\Delta L)]^2/\tau_{\mathrm{eff}} + l^2\phi. \quad (27)$$

Here, τ_{eff} is the effective cycle time defined above, ϕ the hopping rate and $f(\Delta L)$ again the same linear function of ΔL as for the CA-model in the previous section (see Ref. [12] for details).

For short times the population grows exponentially fast while for long times, it grows as $N \propto t^2$. The radius of gyration behaves as $R_{gyr} \propto \sqrt{D_{eff} t}$ which is as in the cellular automaton model provided $[f(\Delta L)]^2/\tau_{eff} \ll l^2\phi$, i.e., if the space gained by diffusion is much larger than the space gained by proliferation. Note, however, that for all parameter choices exponential growth of the radius of gyration cannot be obtained by the FKPP-equation. Hence for dense monolayers, the FKPP-equation does not give a suitable description of the monolayer growth process. However, for the choice shown in Eq. (27) the minimum wave velocity of the deterministic FKPP-equation, $v_{min}^2 = 4(D_{eff}/\tau_{eff})$ behaves qualitatively as the expansion velocity of cell monolayers in the cellular automaton model, for all choices of ϕ, ΔL, τ, and m, i.e., for type I and type II monolayers. To obtain predictions, it must again be taken into account that ΔL and τ are not independent parameters but instead $\Delta L \propto 1/\tau$ (Eq. 7).

4 Discussion

In this paper we have developed a continuum model for dense (type I) monolayers. We used computer simulation results with a lattice-free single-cell-based model introduced recently to explain monolayer growth [37] to guide the development of our continuum model. Our continuum model was based on the following assumptions that we verified by simulations with the lattice-free model: (i) the density within the monolayer is approximately constant, (ii) proliferation is possible only if the local pressure in the tissue is below a threshold value p_0. (iii) The movement of cell mass is triggered by the gradient of pressure.

The resulting model agrees with the cell-based-model in many aspects. Firstly, the initial and asymptotic (long time)-growth regimes for the monolayer radius and the cell population size are the same: after an initial exponential growth regime of both, the radius and the population size, the radius grows linearly and the population size as the square of time. Secondly, for long times the growth velocity of the radius is proportional to the square root of the growth rate. Thirdly, as a consequence of the former issue, the width of the proliferative rim grows as the square root of the cycle time duration.

We remark that our continuum model is similar in form to models developed by other authors [18,46], treating the aggregate as a homogeneous population of cells whose movement is governed by Darcy's law. Unlike most existing models which focus on nutrient availability as the growth-rate limiting process, in our model mechanical effects (and, in particular, contact inhibition) are assumed to regulate the cell proliferation rate. Many of the limitations of the continuum model that we have developed may be addressed by using a multiphase modelling framework to develop new models that can account for cellular heterogeneity and permit the incorporation of alternative descriptions of cell movement [13,19,20,27,50,52]. The models can also be used to investigate the impact on cell proliferation and cell movement of mechanical effects due, for example, to interactions with the tissue in which the tumour is embedded [23,66]. Additionally, it is possible to identify conditions under which the multiphase models predict that a Darcy-type law governs the cell velocity, a result

which places biomechanical models of the type considered in this paper on a stronger foundation.

For monolayers where cell–cell adhesion is weak (type II monolayers), cells close to the boundary detach from the main aggregate and migrate randomly into the extracellular space. In the limit $\sqrt{2dDt} \gg \Delta L$, where ΔL denotes the thickness of the proliferating rim within the main cell aggregate, it is possible to show that the growth process can be described by the FKPP-equation [34]. As ΔL grows, the long time regime can still be modelled as a FKPP-equation if the true diffusion constant D is replace by an effective constant D_{eff} that contains ΔL. However, our studies of dense monolayers show that ΔL is not an independent parameter: it depends on the growth rate via $\Delta L \propto \sqrt{\tau}$ where τ denotes the intrinsic cell cycle duration. Hence, if cell–cell adhesion is negligible, the FKPP equation can be used to model the long-term growth regime if $D \to D_{\text{eff}}$ and $\Delta L_p = c_2\sqrt{\tau}$. We have illustrated, that in the absence of cell–cell adhesion, $v = \hat{c}_1/\sqrt{\tau}$ with $\hat{c}_1 > c_1$ i.e., the free migration accelerates the expansion of the layer. Hence the total thickness of the proliferating rim must be larger in the absence of cell–cell adhesion compared to the case with cell–cell adhesion.

The expansion velocity depends not only on the cycle time τ but also on the sensitivity to contact inhibition through the parameter d_c, and the parameters that determine the shape of the interaction energy such as the cells' Young modulus E and the cells' Poisson number ν and the strength of cell–cell adhesion. In the agent-based lattice-free model discussed in this paper we assumed that cells do not grow anymore if this would lead to a compression of the cell larger than $l - d_c$ with $d_c = 0.75l$ (this is embodied in the interaction potential energy in Fig. 4b and assumption A5). In this case, c_k and $\hat{c}_k$ $k = 1, 2$ depend on E and ν. However, if for different E and ν the growth is triggered by a force or pressure threshold [67] (instead of a compression threshold) then cells with smaller E have a smaller, and cells with larger E a larger d_c, i.e., $d_c(E, \nu)$. Simulations suggest that in this case the kinetics of the population size N is independent of t while the kinetics of the gyration radius R_{gyr} only differs slightly; the difference in the monolayer diameter $L = 2\sqrt{2}R_{gyr}$ for two populations with $E_2 > E_1$ is given by $L_2 - L_1 \approx (d_c(E_2) - d_c(E_1))\sqrt{N}$, ie., a population of cells with a large d_c is less compressed than a population of the same size consisting of cells with a small d_c [37]. Hence in this case c_k and $\hat{c}_k$ become almost independent of E and ν.

In recent work [12] we have shown that a systematic parameter sensitivity analysis of monolayers is feasible using fully parameterised cellular automaton (CA) models while it is not amenable to lattice-free single-cell based models due to the long computation times. The CA-model contains the same parameter ΔL to express the proliferation depth as the FKPP-equation so $\Delta L \propto \sqrt{\tau}$ has to be assumed to facilitate predictions with the CA-model if the duration of the cell cycle changes.

We remark that in future work an exhaustive sensitivity analysis of the three types of models studied in this paper should be performed. This will enable us to identify conditions under which the spatio-temporal behaviour of the models agree (and yield the same predictions) and, hence, to determine how the parameters in the different models are related. Additionally, by performing a more comprehensive search of parameter space we will be able to determine whether the compact radially symmetric growth

seen in the simulations is a persistent feature of the models or whether more irregular, infiltrative spatial structures can arise.

A natural starting point for addressing this issue involves performing a linear stability analysis of the radially symmetric solutions of the continuum model and/or solving the full system of equations (with $0 \leq n \leq 1$), rather than the reduced system (with $n \approx 1$). Similar studies performed on similar continuum models, assuming nutrient-limited growth, have revealed that the choice of the constitutive law used to model the solid tumour plays an important role in its growth characteristics [16,18,28,49]. In particular, if the surface tension effects that maintain cell–cell adhesion of the aggregate are large then the spheroid grows as a compact, spherically symmetric mass. By contrast, if surface tension effects are weak then the symmetry of the tumour boundary is destabilised and irregular, finger-like patterns of invasion are predicted, with budding of the tumour occurring for certain parameter values. Within the lattice-free and lattice-based (CA) single-cell-based models presented in this paper, instabilities of the tumour boundary were not observed for simulations of monolayers in liquid environment. However, computer simulations can naturally capture only limited parameter ranges so we have chosen parameter values consistent with experimental observations.

It is important to notice, that a match of parameters in the whole hierarchy of models composed of continuum models that consider locally averaged cell densities, CA models that consider largely abstract but still single cells and hence permit to represent stochasticity and heterogeneity within cell populations, and more detailed lattice-free single cell models is necessary, to obtain the same predictions with all three model types.

Since the time scales of migration and growth employed in the single-cell based lattice-free model are relative, the same results are obtained if instead of changing the cycle time duration τ at fixed diffusion constant $D = D_0$, the diffusion constant D at fixed τ is modified (Fig. 11).

However, in order to obtain a continuum model that captures the behaviour of a growing monolayer for all values of cell–cell adhesion (including the absence of cell–
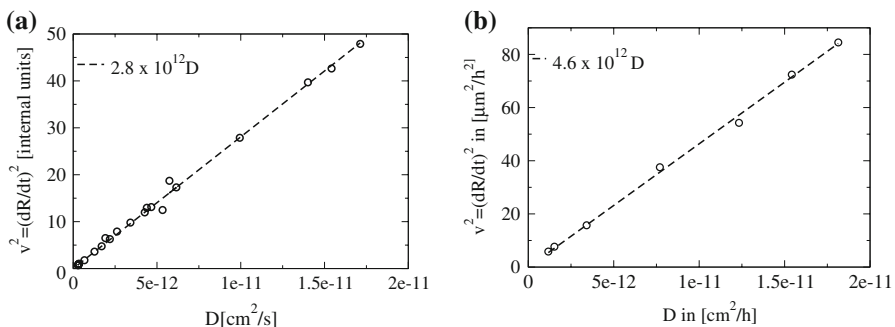

Fig. 11 **a** Square of expansion velocity for type I monolayers as a function of D. The figures shows $v^2 \propto D$. D can be linked to the cell motility $\tilde{\mu}$ by $D \propto \tilde{\mu} F_T$, where $\gamma = \tilde{\mu}^{-1}$ denotes the effective friction [38]. Increasing the cell motility has the same effect as increasing the cell cycle duration since in both cases the cells have more time to escape the mechanical compression forces exerted by their neighbour cells and hence can more easily relax mechanical stress. Hence, $v^2 \propto \tilde{\mu}/\tau$. **b** Expansion velocity as a function of D for type II monolayers. (Results obtained by simulations with the individual-based off-lattice model.)

cell adhesion) and for all D and τ for short and long times, the continuum model we derived in this paper for type I monolayers must be extended to obtain an equation that captures the behaviour of the FKPP-equation in the limit of sparse (type II) monolayers. From our above studies we propose that the following set of equations, containing a diffusion term, be analysed:

$$\frac{\partial n(\underline{r}, t)}{\partial t} + \nabla \cdot \left(n(\underline{r}, t)\underline{v}\right) - \nabla \cdot (D\nabla n) = s_0 n H(p_0 - p), \tag{28}$$

$$\underline{v} = -\mu \nabla p, \tag{29}$$

$$\frac{\partial R}{\partial t} = \underline{v} \cdot \hat{\underline{n}}\big|_{r=R}. \tag{30}$$

where $H(p_0 - p)$ is again the Heaviside (step) function and D the diffusion constant. If the cell density is at its saturation value, $n = n^*$, then the model for dense one-cell-thick monolayers studied above emerges. On the other hand, in the absence of cell–cell adhesion and sufficiently large D the density is very small and each cell is almost isolated in space so that $p \ll p_0 \approx const$. In this case, $\partial_t n \approx s_0 n + D\nabla^2 n$. If within the monolayer interior the density increases, then cells get into contact, $p \to p_0$, so that eventually $H(p_0 - p) = 0$ and no further cell division is possible. This model should be studied in a subsequent paper but needs to be closed by a proper law $p(n)$.

We finally like to stress that the results found in this paper also hold for three-dimensional cell aggregates for which computer-simulations suggest the same form of contact inhibition [37].

Appendix A: Parameters in the agent-based lattice-free model

Here we explain how the cycle time and the diffusion constant are linked to the step sizes in the Metropolis algorithm-approach. The intrinsic cycle time duration is defined by

$$\tau = \frac{n_g l \Delta t}{\delta a_{max}/2} = \frac{n_g l \Delta t}{\delta a_{max}/2} \Rightarrow \Delta \hat{t} \equiv \frac{\Delta t}{\tau} = \frac{\delta \hat{a}_{max}}{2 n_g}. \tag{31}$$

Note, that the true cycle time can be larger than this if cell–cell interactions delay the growth or division of a cell.

The diffusion constant is:

$$\hat{D} = \frac{\langle (\delta \hat{\underline{r}})^2 \rangle}{2d \Delta \hat{t}} = \frac{(k \hat{\xi}_{max}^2)}{(2d \Delta \hat{t})} \tag{32}$$

$\hat{D} = D\tau/l^2$ is the dimensionless diffusion constant, $k = 1/2$ in $d = 2$ (and $k = 2/5$ in $d = 3$).

The parameters have been determined as follows.

– The reference diffusion constant D_0, the cell diameter l and the cycle time τ have been chosen [typically $D \approx 1.3 \times 10^{-11}$ cm^2/s and $\tau \approx 19$ h (Bru, private communication)].
– Equation 31 is inserted into Eq. 32.
– The parameters $\delta\hat{a}_{\max} \ll 1$ (≈ 0.02) and $n_g \gg 1$ are chosen, which, together with D, determine $\hat{\xi}^2_{\max}$. $\hat{\xi}_{\max}(\delta a_{\max}, n_g, \hat{D})$ was chosen sufficiently small ($\ll 1$) in order to obtain a linear velocity–force relationship (i.e., increasing the applied force by a certain factor increases the migration velocity by the same factor).

In case of purely active movement, the speed of the intracellular re-organisation processes is expected to limit the migration velocity which we assume is not the case for the migration velocities considered here. Notice also, that the choice of $\delta\hat{a}_{\max}$ and n_g, together with τ also determines $\Delta\hat{t}$, which denotes the period of time between two successive move trials.

For three-dimensional simulations with the agent-based lattice-free model rotations around three space-fixed axes by an angles $\delta\alpha_i$ with $i = 1, 2, 3$ according to the algorithm of Barker and Watts (see Ref. [5]) are considered.

Appendix B: Multicellular aggregates in three dimensions

As shown in Refs. [37,39], the comparison of computer simulation results with published experimental data suggest that for three-dimensional multicellular spheroids growing in suspension the growth kinetics may be determined by the same form of biomechanical contact inhibition as for dense monolayers. The growth kinetics for multicellular spheroids suggested an initial growth regime in which the population size $N(t)$ and the aggregate diameter $L(t)$ satisfy $N(t) \propto e^{t/\tau}$ and $L(t) \propto e^{t/3\tau}$. For long times, we found $N(t) \propto t^3$ (in d dimensions, t^d) and $L(t) \propto t$. In this case, negligible changes in the system's growth kinetics were detected in response to a 20-fold change in the concentration of nutrient in the culture medium.

The results for the continuum model in this case are similar to those presented in Sect. 2.2 for 2D growth. In particular we find that for case 1 (i.e., $p < p_0$ for $0 < r < R(t)$)

$$p(r, t) = \frac{\gamma}{R} + \frac{s_0}{6\mu}(R^2 - r^2),$$

$$R(t) = R(t = 0)e^{s_0 t/3},$$

$$N(t) \simeq e^{s_0 t}.$$

Case 1 persists until $R = R_{cr}$ where R_{cr} is the larger positive root of the following cubic:

$$0 = R_{cr}^3 - \frac{6\mu p_0}{s_0}R_{cr} + \frac{6\mu\gamma}{s_0}.$$

If $R > R_{cr}$ then the above solution breaks down and cells in the central region of the cluster (where $0 < r < R_p(t)$) become contact-inhibited from proliferating and the system evolves to case 2.

Case 2: here we require $p < p_0$ for $r \in (R_p, R)$ and $p \geq p_0$ for $r \in (0, R_p)$

$$p(r, t) = \begin{cases} p_0 & 0 < r < R_p \\ p_0 - \frac{s_0}{6\mu}(r^2 - R_p^2) + \frac{s_0 R_p^3}{3\mu}\left(\frac{1}{R_p} - \frac{1}{r}\right) \end{cases}$$

wherein $R(t)$ and $R_p(t)$ together solve the following ODE and algebraic equations:

$$\frac{dR}{dt} = \frac{s_0}{3R^2}(R^3 - R_p^3),$$

$$\frac{\gamma}{R} = p_0 - \frac{s_0}{6\mu}(R^2 - R_p^2) + \frac{s_0 R_p^3}{3\mu}\left(\frac{1}{R_p} - \frac{1}{r}\right).$$

The long time behaviour is determined as for the 2D case: we rescale the independent and dependent variables as follows:

$$t = \frac{\tau}{\epsilon}, \quad R(t) = \frac{\bar{R}(\tau)}{\epsilon}, \quad R_p(t) = \frac{\bar{R}(\tau)}{\epsilon} - R_{p1} + \epsilon R_{p2}.$$

At leading order we recover

$$\bar{R}(\tau) = R^* + \sqrt{\frac{6\mu s_0 p_0}{7}}\tau \quad \text{and} \quad R_{p1}(\tau) = \sqrt{\frac{6\mu p_0}{7s_0}}, \quad \text{constant},$$

wherein R^* is a constant.

References

1. Adam J, Belomo N (1997) A survey of models for tumor-immune system dynamics. Birkhäuser, Boston
2. Alarcon T, Byrne H, Maini P (2004) A mathematical model of the effects of hypoxia on the cell-cycle of normal and cancer cells. J Theor Biol 229:395–411
3. Alber MS, Kiskowski MA, Glazier JA, Jiang Y (2002) On cellular automaton approaches to modeling biological cells. In: Rosenthal J, Gilliam DS (eds) Mathematical systems theory in biology, communication, and finance, IMA 142. Springer, New York, pp 1–40
4. Alcaraz J, Buscemi L, Grabulosa M, Trepat X, Fabry B, Farre R, Navajas D (2003) Microrheology of human lung epithelial cells measured by atomic force microscopy. Biophys J 84:2071–2079
5. Allen M, Tildersley D (1987) Computer Simulation of Liquids. Oxford Science Publications, Oxford
6. Ambrosi D, Mollica F (2002) On the mechanics of a growing tumor. Int J Eng Sci 40(12): 1297–1316
7. Ambrosi D, Mollica F (2004) The role of stress in the growth of a multicell spheroid. J Math Biol 48(5):477–479
8. Anderson A, Chaplain MAJ, Rejniak K (2007) Single-cell-based models in biology and medicine. Birkhäuser, Basel
9. Anderson A, Chaplain MAJ, Newman E, Steele R, Thompson A (2000) Mathematical modeling of tumor invasion and metastasis. J Theor Med 2:129–154

10. Araujo R, McElwain D (2004) A history of the study of solid tumour growth: the contribution of mathematical models. Bull Math Biol 66:1039–1091
11. Beysens D, Forgacs G, Glazier J (2000) Cell sorting is analogous to phase ordering in fluids. Proc Natl Acad Sci USA 97(17):9467–9471
12. Block M, Schoell E, Drasdo D (2007) Classifying the expansion kinetics and critical surface dynamics of growing cell populations. Phys Rev Lett 99:248,101–248,104
13. Breward C, Byrne H, Lewis C (2002) The role of cell–cell interactions in a two-phase model for avasular tumour growth. J Math Biol 45:125–152
14. Bru A, Albertos S, Subiza J, Garcia-Arsenio J, Bru I (2003) The universal dynamics of tumor growth. Biophys J 85:2948–2961
15. Bru A, Pastor J, Fernaud I, Bru I, Melle S, Berenguer C (1998) Super-rough dynamics of tumor growth. Phys Rev Lett 81(18):4008–4011
16. Byrne H (1997) The importance of intercellular adhesion in the development of carcinomas. IMA J Math Appl Med Biol 14:305–323
17. Byrne H, Chaplain J (1996) Modelling the role of cell–cell adhesion in the growth and development of carcinomas. Math Comput Model 12:1–17
18. Byrne H, Chaplain M (1997) Free boundary value problem associated with the growth and development of multicellular spheroids. Eur J Appl Math 8:639–658
19. Byrne HM, King JR, McElwain DLS, Preziosi L (2003) A two-phase model of solid tumor growth. Appl Math Lett 16(4):567–573
20. Byrne H, Preziosi L (2003) Modelling solid tumour growth using the theory of mixtures. Math Med Biol 20:341–366
21. Carpick R, Ogletree DF, Salmeron M (1999) A gerneral equation for fitting contact area and friction vs load measurements. J Colloid Interface Sci 211:395–400
22. Chaplain M, Graziano L, Preziosi L (2006) Mathematical modelling of the loss of of tissue compression responsiveness and its role in solid tumour development. Math Med Biol 23(3):197–229
23. Chen C, Byrne H, King J (2001) The influence of growth-induced stress from the surrounding medium on the development of multicell spheroids. J Math Biol 43:191–220
24. Chesla S, Selvaraj P, Zhu C (1998) Measuring two-dimensional receptor-ligand binding kinetics by micropipette. Biophys J 75:1553–1557
25. Chu YS et al (2005) Johnson–Kendall–Roberts theory applied to living cells. Phys Rev Lett 94: 028,102
26. Cickovski T, Huang C, Chaturvedi R, Glimm T, Hentschel H, Alber M, Glazier JA, Newman SA, Izaguirre JA (2005) A framework for three-dimensional simulation of morphogenesis. IEEE/ACM Trans Comput Biol Bioinformatics 2(3):273–288
27. Please CP, Pettet G, McElwain D (1998) A new approach to modelling the formation of necrotic regions in tumours. Appl Math Lett 11:89–94
28. Cristini V, Lowengrub J, Nie Q (2003) Nonlinear simulations of tumor growth. J Math Biol 46: 191–224
29. Dallon J, Othmer H (2004) How cellular movement determines the collective force generated by the dictyostelium discoideum slug. J Theor Biol 231:203–222
30. DeMasi A, Luckhaus S, Presutti E (2005) Two-scale hydrodynamic limit for a model of malignant tumor cells. MPI-MIS (Preprint) 2:1–47
31. Dormann S, Deutsch A (2002) Modeling of self-organized avascular tumor growth with a hybrid cellular automaton. In Silico Biol 2:0035
32. Drasdo D (1996) Different growth regimes found in a monte-carlo model of growing tissue cell populations. In: Schweitzer F (ed) Self organization of complex structures: from individual to collective dynamics. Gordon & Breach, New York, pp 281–291
33. Drasdo D (2003) On selected individual-based approaches to the dynamics of multicellular systems. In: Alt W, Chaplain M, Griebel M (eds) Multiscale modeling. Birkhäuser, Basel
34. Drasdo D (2005) Coarse graining in simulated cell populations. Adv Complex Syst 8(2 & 3): 319–363
35. Drasdo D (2008) Center-based single-cell models: an approach to multi-cellular organization based on a conceptual analogy to colloidal particles. In: Anderson A, Chaplain M, Rejniak K (eds) Single-cell-based models in biology and medicine. Birkhäuser, Basel (in press)
36. Drasdo D, Forgacs G (2000) Modelling the interplay of generic and genetic mechanisms in cleavage, blastulation and gastrulation. Dev Dyn 219:182–191

37. Drasdo D, Hoehme S (2005) A single-cell based model to tumor growth in-vitro: monolayers and spheroids. Phys Biol 2:133–147
38. Drasdo D, Hoehme S, Block M (2007) On the role of physics in the growth and pattern formation of multi-cellular systems: What can we learn from individual-cell based models? J Stat Phys 128(1 & 2): 319–363
39. Drasdo D, Höhme S (2003) Individual-based approaches to birth and death in avascular tumors. Math Comput Model 37:1163–1175
40. Drasdo D, Kree R, McCaskill J (1995) Monte-carlo approach to tissue-cell populations. Phys Rev E 52(6):6635–6657
41. Friedman A (2007) Mathematical analysis and challenges arrising from models of tumor growth. Math Model Methods Appl Sci 17:1751–1772
42. Galle J, Aust G, Schaller G, Beyer T, Drasdo D (2006) Single-cell based mathematical models to the spatio-temporal pattern formation in multi-cellular systems. Cytometry A (in press)
43. Galle J, Loeffler M, Drasdo D (2005) Modelling the effect of deregulated proliferation and apoptosis on the growth dynamics of epithelial cell populations in vitro. Biophys J 88:62–75
44. Galle J, Sittig D, Hanisch I, Wobus M, Wandel E, Loeffler M, Aust G (2006) Individual cell-based models of tumor-environment interactions: multiple effects of cd97 on tumor invasion. J Am Path 169(5):1802–1811
45. Graner F, Glazier J (1992) Simulation of biological cell sorting using a two-dimensional extended potts model. Phys Rev Lett 69(13):2013–2016
46. Greenspan H (1976) On the growth and stability of cell cultures and solid tumors. J Theor Biol 56(1):229–242
47. Hogeweg P (2000) Evolving mechanisms of morphogenesis: on the interplay between differential adhesion and cell differentiation. J Theor Biol 203:317–333
48. Johnson K, Kendall K, Roberts A (1971) Surface energy and the contact of elastic solids. Proc R Soc A 324:301–313
49. King J, Franks S (2004) Mathematical analysis of some multidimensional tissue-growth models. Eur J Appl Math 15(3):273–295
50. Landman K, Please C (2001) The influence of growth-induced stress from the surrounding medium on the development of multicell spheroids. J Math Biol 43:191–220
51. Preziosi L (2003) Cancer modelling and simulation. Chapman & Hall/CRC Press, London/West Palm Beach
52. MacArthur B, Please C (2004) Residual stress generation and necrosis formation in multicell tumour spheroids. J Math Biol 49:537–552
53. Mahaffy R, Shih C, McKintosh F, Kaes J (2000) Scanning probe-based frequency-dependent micro-rheology of polymer gels and biological cells. Phys Rev Lett 85:880–883
54. Merks R, Glazier J (2005) A cell-centered approach to developmental biology. Physica A 352:113–130
55. Metropolis N, Rosenbluth A, Rosenbluth M, Teller A, Teller E (1953) Equation of state calculations by fast computing machines. J Chem Phys 21:1087–1092
56. Lekka M, Laidler P, Gil D, Lekki J, Stachura Z, Hrynkiewicz AZ (1999) Elasticity of normal and cancerous human bladder cells studied by scanning force microscopy. Eur Biophys J 28(4): 312–316
57. Mombach J, Glazier J (1996) Single cell motion in aggregates of embryonic cells. Phys Rev Lett 76(16):3032–3035
58. Moreira J, Deutsch A (2002) Cellular automata models of tumour development—a critical review. Adv Complex Syst 5(1):247–267
59. Nelson CM, Jean RP, Tan JL, Liu WF, Sniadecki NJ, Spector AA, Chen CS (2005) Proc Natl Acad Sci USA 102:11594–11599
60. Newman T (2005) Modeling multi-cellular systems using sub-cellular elements. Math Biosci Eng 2(3):613–624
61. Palsson E, Othmer H (2000) A model for individual and collective cell movement in dictyostelium discoideum. Proc Natl Acad Sci USA 12(18):10,448–10,453
62. Piper J, Swerlick R, Zhu C (1998) Determining force dependence of two-dimensional receptor-ligand binding affinity by centrifugation. Biophys J 74:492–513
63. Preziosi L, Tosin A, Multiphase modeling of tumor growth and extracellular matrix interaction: mathematical tools and applications. J Math Biol
64. Ramis-Conde I, Chaplain MAJ, Anderson A (2008) Mathematical modelling of cancer cell invasion of tissue. Math Comput Model (in press)

65. Roose T, Chapman S, Maini P (2007) Mathematical models of avascular tumour growth: a review. SIAM Rev 49(2):179–208
66. Roose T, Netti PA, Munn L, Boucher Y, Jain R (2003) Solid stress generated by spheroid growth estimated using a linear poroelasticity model. Microvasc Res 66:204–212
67. Schaller G, Meyer-Hermann M (2005) Multicellular tumor spheroid in an off-lattice voronoi-delaunay cell model. Phys Rev E 71:051,910-1–051,910-16
68. Schienbein M, Franke K, Gruler H (1994) Random walk and directed movement: comparison between inert particles and self-organized molecular machines. Phys Rev E 49(6):5462–5471
69. Schiffer I, Gebhard S, Heimerdinger C, Heling A, Hast J, Wollscheid U, Seliger B, Tanner B, Gilbert S, Beckers T, Baasner S, Brenner W, Spangenberg C, Prawitt D, Trost T, Schreiber W, Zabel B, Thelen M, Lehr H, Oesch F, Hengstler J (2003) Switching off her-2/neu in a tetracycline-controlled mouse tumor model leads to apoptosis and tumor-size-dependent remission. Cancer Res 63:7221–7231
70. Stevens A (2000) The derivation of chemotaxis equations as limit dynamics of moderately interacting stochastic many-particle systems. SIAM J Appl Math 61(1):183–212
71. Stott E, Britton N, Glazier J, Zajac M (1999) Stochastic simulation of benign avascular tumor growth using the potts model. Math Comput Model 30:183–198
72. Ward J, King J (1997) Mathematical modelling of avascular-tumor growth. IMA J Math Appl Med Biol 14:39–69